Multilevel Torque Hysteresis-Band Based Direct-Torque Control Strategy for a Three-Level Open-End Winding Induction Motor Drive for Electric Vehicle Applications

Suresh Lakhimsetty, Venkata Siva Prasad Satelli, Rajendra Singh Rathore, and V. T. Somasekhar, *Member, IEEE*

***Abstract*— The number of levels present in the torque-hysteresis controller influence the performance of the direct torque controlled (DTC) induction motor drives. In this paper, the effects of the number of levels in the torque-hysteresis-band controllers (THBCs) on the performance of the conventional DTC-based three-level open-end winding induction motor drives are reported. A power-loss evaluation model was employed to investigate the influence of the number of levels present in THBC on the switching and conduction losses occurring in the dual-inverter system. The performance indices considered in this paper are: 1) the flux-ripple; 2) the torque ripple; and 3) the total power loss in the dual-inverter system. Furthermore, these performance indices are evaluated with a newly emerging control strategy, namely, the predictive torque control, and are compared with those obtained with the DTC. The simulation results are validated by showing the experimental results.**

***Index Terms*— Direct torque control (DTC), flux ripple, open-end winding induction motor (OEWIM), predictive torque control (PTC), torque-hysteresis-band controller (THBC), torque ripple.**

I. Introduction

In THE recent past, multilevel inverters (MLIs) have registered a good penetration into applications such as electric vehicles, renewable energy sources, rolling mills, propulsion systems, high-voltage direct current transmission, and the like [1], [2]. The advantages of MLIs include: 1) achievement of higher ac voltages with semiconductor switching devices of lower voltage ratings; 2) reduced common mode voltages; 3) enhanced spectral performance [reduced total harmonic distortion (THD)] as output voltages are near sinusoidal; 4) low dv/dt on the semiconductor devices and low electromagnetic interference; 5) smaller or no requirement of filters; and 6) reduction in the winding insulation stress compared to the two-level (2L) voltage source inverters [3]. The most popular MLI circuit configurations reported in the literature are: 1) neutral point clamped MLI; 2) flying capacitor (FC) MLI; and 3) cascaded H-bridge (CHB) MLI [4]. However, the main drawbacks associated with these topologies are: 1) deviation in the neutral point voltage in the case of NPC MLI; 2) requirement of special control circuitry to balance the floating capacitor voltages in the FC MLI; and 3) requirement of increased isolated dc power supplies in CHB MLI for higher voltage levels.

In the recent past, a new member is added to the family of MLIs called as open-end winding induction motor (OEWIM) drive [5]. Unlike the other topologies, wherein the inverter and the drive are considered as two separate entities, in the OEWIM drive (OEWIMD), the motor is an integral part of the drive system. The drawbacks associated with the aforementioned topologies are avoided with the OEWIM topology. The advantages associated with the OEWIM are: 1) conventional two 2L voltage source inverters (C2-LIs) are sufficient to realize open end winding topology and 2) more redundancy in the space vector switching states, which makes it amenable for the development of several new pulsewidth modulation (PWM) schemes [5]–[10].

Another advantage with the OEWIMD topology, when compared to the other MLIs is that it may be operated as a hybrid MLI, as the constituent 2L voltage source inverters (VSIs) can be fed with isolated dc-voltage sources. These sources can be either batteries, ultracapacitors, fuel cells, or photovoltaic arrays. This feature makes the OEWIMD suitable for the electric vehicles (EVs), hybrid EVs, and water pumping applications [11]–[16].

The motor drive industry had recognized the potential of the direct torque control (DTC) and developed it to become the leading technology in the arena of induction motor drives. Unlike the field-oriented control (FOC), its main contender,

Manuscript received March 2, 2018; revised May 6, 2018, July 8, 2018, and August 21, 2018; accepted September 1, 2018. Date of publication September 17, 2018; date of current version July 31, 2019. Recommended for publication by Associate Editor Antonio J. Marques Cardoso. *(Corresponding author: Suresh Lakhimsetty.)*

S. Lakhimsetty and V. T. Somasekhar are with the Department of Electrical Engineering, National Institute of Technology, Warangal 506004, India (e-mail: suresh.201@gmail.com; vtsomsekhar@rediffmail.com).

V. S. P. Satelli was with the Department of Electrical Engineering, National Institute of Technology, Warangal 506004, India. He is now with IE Power Technologies Private Limited, Bengaluru 560058, India. (e-mail: sivaprasadsatelli@gmail.com).

R. S. Rathore was with the Department of Electrical Engineering, National Institute of Technology, Warangal 506004, India. He is now with Bombardier Transportation, Hyderabad 500032, India (e-mail: rsrathore2007@gmail.com).

Color versions of one or more of the figures in this paper are available online at http://ieeexplore.ieee.org.

Digital Object Identifier 10.1109/JESTPE.2018.2870382

DTC is insensible to the variation of motor parameters and results in a better dynamic response of torque. In addition, DTC is much simpler in terms of implementation as it does not need coordinate transformation, field orientation, complicated tuning associated with inner current loops and issues concerning the decoupling of 'q' and 'd' variables [17]–[20].

Several variants of the DTC strategies are reported in the literature, which are classified as: 1) voltage-vector selection using switching table [21] (called as conventional DTC technique), 2) direct self-control [22], and 3) space-vector modulation [23]. Among these strategies, the voltage vector selection using switching table has become very popular and was mostly adopted in all industrial applications because of its simplicity and ease of implementation. Also, the problem associated with the implementation of over-modulation technique (which is unavoidable with space vector PWM technique) is absent in this scheme.

All of the aforementioned DTC strategies aim the improvisation of performance of induction motor drives, wherein the reduction of torque ripple is an important aspect. The available literature is rich in terms of the implementation of these strategies with the C2-LIs. Extension of these techniques to MLIs is cumbersome, because of the complexity in the voltage vector selection as the number levels increase.

Model predictive control (MPC) techniques, which are relatively recent, are very promising for applications pertaining to the control of power converters and motor drives [24]. Predictive torque control (PTC) which falls in the gamut of MPC techniques in an alternative to the DTC techniques so for as the motor drive applications is concerned [24], [25]. In PTC, the future behavior of the motor flux and torque is predicted by using the motor model. Unlike the FOC technique, DTC and PTC do not use any modulator. While the DTC technique chooses the voltage vector based on the flux and torque errors, the PTC technique selects the optimal voltage vector based on the optimization of a cost function. In general, the cost function includes the error in torque and flux with appropriate weighting factors. The performance of the cost function is affected by the number of constraints in it and their respective weighting factors. Different techniques are suggested in the available literature to address the issue of selecting the weighting factor [26]–[30]. Recently, the conventional PTC technique was extended to the 4L OEWIMD with normalized weighted sum model [31], and the elimination of weighting factor [32].

In this paper, the conventional DTC (i.e., voltage vector selection using switching table) and PTC techniques are applied to the 3L OEWIMD. The comparative performance is carried out by employing: 1) the 3L torque hysteresis band controller (3L-THBC); 2) the 5L torque hysteresis band controller (5L-THBC); 3) the 7L torque hysteresis band controller (7L-THBC) (all for the DTC technique); and 4) the PTC technique. The three THBCs are designed in such a way that the dual-inverter system is operated as a 2L inverter at lower speeds, to reduce the dual inverter loss. Furthermore, the effects of DTC and PTC techniques on the torque ripple, the flux ripple, the total power loss in the dual inverter system, and the dv/dt in motor phase voltage are also investigated.

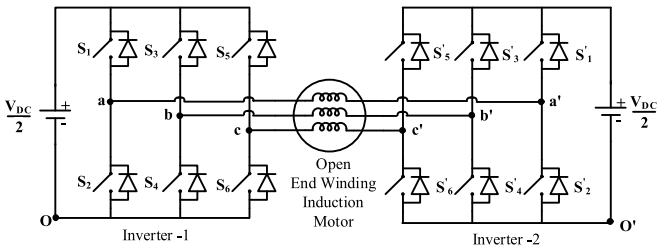

Fig. 1. 3L dual-inverter fed OEWIM.

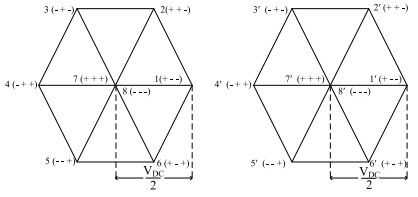

Fig. 2. Space vector locations of inverter 1 (left) and inverter 2 (right).

The comparative evaluation of the abovementioned THBC-based DTC and PTC OEWIMD is carried out by considering the performance indices such as torque-ripple, flux-ripple, voltage THD, no-load current THD, dual inverter loss, and the efficiency of the dual-inverter system. The performance of the conventional 2L VSI fed induction motor drive with DTC is based as the reference (i.e., bench mark), for the comparative evaluation of performance of all the aforementioned control strategies. Finally, the experimental results are presented to validate the simulation results.

II. Three-Level Open-End Winding Induction Motor Drive

The circuit diagram for the realization of the 3L OEWIMD is shown in Fig. 1. An induction motor with open stator windings is fed from either end by two conventional 2L inverters, which have equal dc-link voltages (Fig. 1). An OEWIMD, operated with two isolated dc-power supplies, would have its zero-sequence voltage blocked across the points "O" and "O′" (Fig. 1). Despite the presence of the zero-sequence voltage, no zero-sequence current can flow in this circuit, as there is no path for it.

Each individual inverter of the OEWIMD possesses eight space vectors as shown in Fig. 2. The resultant space vector diagram of the dual-inverter system is shown in Fig. 3, which possesses a total of 64 space vector combinations. The pole voltages of individual inverters of the dual-inverter system (v_{aO} and $v_{a'O'}$) are toggled between the values of 0 and $V_{\mathrm{DC}}/2$, the resultant phase voltage of OEWIMD having three levels across it, as shown in Table I.

The mathematical model of OEWIM can be explained by using Fig. 4. The inputs for the model are switching pulses from switching table and dc-link voltage. V_{aO}, V_{bO}, V_{cO} are pole voltages of inverter 1 and $v_{a'O'}$, $v_{b'O'}$, $v_{c'O'}$ are pole voltages of inverter 2.

The difference of pole voltages is obtained by subtracting the pole voltages of inverter 2 from inverter 1. As both

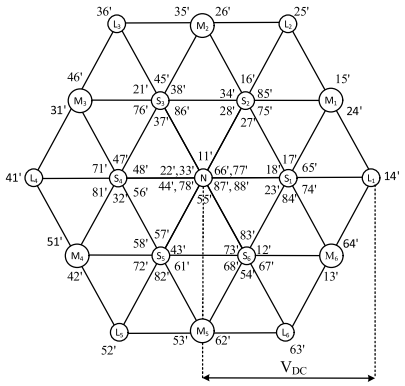

Fig. 3. Space vector combination of dual-inverter scheme.

TABLE I
VOLTAGE LEVELS IN OEWIMD

Pole Voltage of Inverter-1 (v_{aO})	Pole Voltage of Inverter-2 ($v_{a'O}$)	Phase Voltage ($v_{aa'} = v_{aO} - v_{a'O'}$)
$V_{DC}/2$	0	$V_{DC}/2$
0	0	0
$V_{DC}/2$	$V_{DC}/2$	
0	$V_{DC}/2$	$-V_{DC}/2$

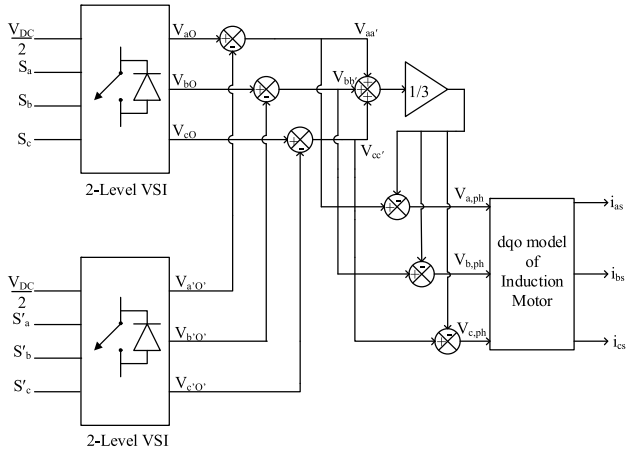

Fig. 4. Modeling of OEWIMD.

inverters are fed by isolated dc supplies, the zero sequence voltages (common mode voltages) appear across the point's O and O'. Motor phase voltages can be obtained by subtracting the common mode voltages from difference in the pole voltages [33].

The difference of pole voltages (assuming that the points O and O' are connected together) is given by

$$v_{aa'} = v_{aO} - v_{a'O'} \tag{1}$$

$$v_{bb'} = v_{bO} - v_{b'O'} \tag{2}$$

$$v_{cc'} = v_{cO} - v_{c'O'}. \tag{3}$$

Zero-sequence voltages are defined as

$$v_{OO'} = \frac{1}{3}(v_{aa'} + v_{bb'} + v_{cc'}). \tag{4}$$

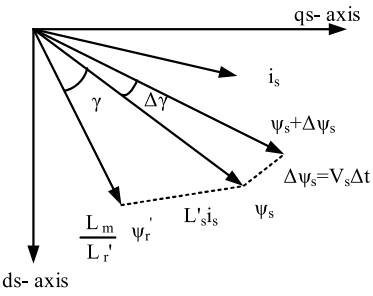

Fig. 5. Stator flux, rotor flux, and stator current vectors on $d_s q_s$ plane (stator resistance neglected).

The phase voltages of the OEWIM for an isolated power supply is determined by

$$v_{a,\mathrm{ph}} = v_{aa'} - v_{OO'} \tag{5}$$

$$v_{b,\mathrm{ph}} = v_{bb'} - v_{OO'} \tag{6}$$

$$v_{c,\mathrm{ph}} = v_{cc'} - v_{OO'}. \tag{7}$$

Writing (5)–(7) in the matrix form

$$\begin{bmatrix} v_{a,\mathrm{ph}} \\ v_{b,\mathrm{ph}} \\ v_{c,\mathrm{ph}} \end{bmatrix} = \frac{1}{3}\begin{bmatrix} 2 & -1 & -1 \\ -1 & 2 & -1 \\ -1 & -1 & 2 \end{bmatrix}\begin{bmatrix} v_{aa'} \\ v_{bb'} \\ v_{cc'} \end{bmatrix} \tag{8}$$

$$\begin{bmatrix} v_{a,\mathrm{ph}} \\ v_{b,\mathrm{ph}} \\ v_{c,\mathrm{ph}} \end{bmatrix} = \frac{1}{6}\begin{bmatrix} 2 & -1 & -1 \\ -1 & 2 & -1 \\ -1 & -1 & 2 \end{bmatrix}\begin{bmatrix} S_a - S_{a'} \\ S_b - S_{b'} \\ S_c - S_{c'} \end{bmatrix} V_{\mathrm{DC}} \tag{9}$$

where S_a, S_b, and S_c are switching pulses to inverter 1 and $S_{a'}$, $S_{b'}$, $S_{c'}$ are switching pulses to inverter 2.

Quadrature components of motor phase voltages in the stationary frame of reference are given as

$$v_{\alpha s} = 3v_{a,\mathrm{ph}}/2 \tag{10}$$

$$v_{\beta s} = (\sqrt{3}/2)(v_{b,\mathrm{ph}} - v_{c,\mathrm{ph}}). \tag{11}$$

III. DIRECT TORQUE CONTROL STRATEGY

The DTC in induction motor drives is accomplished by controlling two voltage components namely, the flux component V_{ds} and the torque component V_{qs}, which are mutually perpendicular to each other as shown in Fig. 5 [34]. The DTC achieves a quick and precise torque response in induction motor drives. The instantaneous values of flux and torque are calculated from the measured values (voltage and current) and then controlled directly by selecting the optimal switching vectors. The brief description of DTC is explained as follows [34].

The torque expression for induction motor can be expressed as

$$\overline{T_e} = (2/3)\,(P/2)\,\left(\overline{\psi}_s \times \overline{I}_s\right) \tag{12}$$

where ψ_s and I_s are stator flux and currents, respectively, and the simplified torque equation in terms of machine parameters, stator flux, and rotor flux is given as

$$\overline{T}_e = (2/3)\,(P/2)\,\left(L_m/\left(L_r L_s'\right)\right)\,|\overline{\psi_s}||\overline{\psi_r}|\sin\gamma \tag{13}$$

where $\overline{\psi_s}$ and $\overline{\psi_r}$ are the stator and rotor flux vectors (both fixed to the stationary reference frame), L_m is the

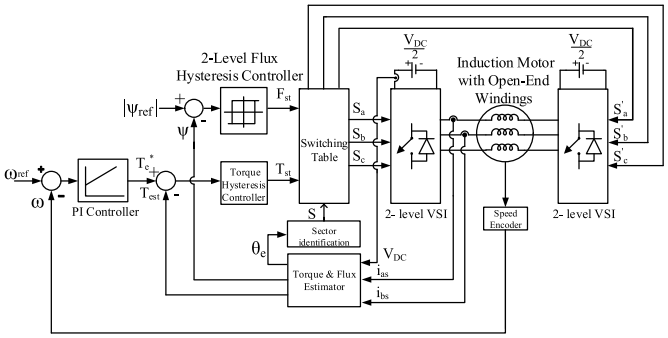

Fig. 6. DTC of 3L OEWIM with THBC.

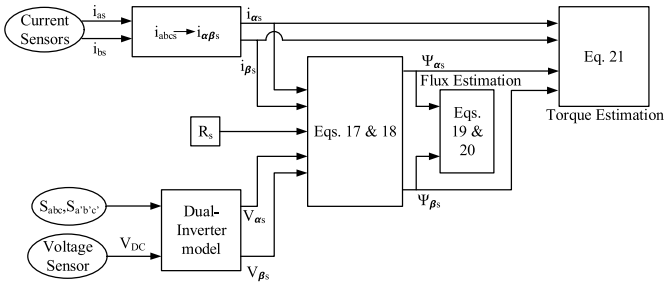

Fig. 7. Mathematical representation of stator flux and torque estimation.

magnetizing inductance, L_s' is a measure of the stator inductance, L_r is the rotor inductance, P is the number of poles, and γ is the angle between the stator and rotor fluxes.

If the rotor flux remains constant and stator flux is changed incrementally by stator voltage V_s (see Fig. 5) and the corresponding change of torque angle (γ) is $\Delta\gamma$, the incremental torque ΔT_e expression is given as

$$\overline{\Delta T_e} = \frac{2}{3}\frac{P}{2}\frac{L_m}{L_r L_s'}|\overline{\psi_r}||\overline{\psi_s} + \Delta\overline{\psi_s}|\sin(\Delta\gamma). \tag{14}$$

Thus, the developed torque mainly depends on the stator flux and the angle between the stator flux and rotor flux, as the rotor flux vector moves slowly compared to the stator flux.

IV. THBC-Based DTC Strategy for Three-Level OEWIMD

The conventional DTC has its own advantages when compared to the FOC. However, the disadvantages associated with the standard 2L DTC drive are: higher torque ripple and switching losses because of the hysteresis band controller and the selection of small voltage source vectors. Also, the variable switching frequency of the inverter inherently affects the shaft torque and produces the more torque harmonics.

Using the freedom of the space vector redundancy in the 3L OEWIMD, a new lookup table-based conventional DTC strategy is proposed, by introducing more levels in the THBC to avoid the abovementioned drawbacks. The levels in the THBC are chosen as: 1) 3L-THBC; 2) 5L-THBC; and 3) 7L-THBC.

The closed-loop DTC block diagram of direct torque and flux control with the proposed THBC for 3L OEWIMD is shown in Fig. 6. From Fig. 6, it is evident that the control block diagram is similar to the one, which uses 2L voltage source inverter. However, the modifications are made in terms of the number of levels in the THBC. The quantities sensed for the estimation of flux and torque are: phase currents (i_{as}, i_{bs}), dc-link voltage ($V_{\rm DC}$), switching pulses ($S_{a,b,c}$, $S_{a',b',c'}$) of the dual-inverter system, per phase stator resistance (R_s) and the rotor speed of OEWIMD (ω), as shown in Fig. 6.

As explained earlier, the OEWIMD have a total of 64 space vector combinations spread over 19 space vector locations. These 19 space vector locations are grouped into the following categories: 1) null vector (N); 2) small vectors (S_x); 3) medium vectors (M_x); and 4) large vectors (L_x), where $x\epsilon$(1, 2, 3, 4, 5, and 6) as shown in Fig. 3.

Using the open-end winding induction motor dq_0 model in Section III and from the motor side information, the stator voltages can be represented in form of stator flux components as [34]

$$\upsilon_{\alpha s} = R_s i_{\alpha s} + \frac{d}{dt}\psi_{\alpha s} \tag{15}$$

$$\upsilon_{\beta s} = R_s i_{\beta s} + \frac{d}{dt}\lambda\psi_{\beta s}. \tag{16}$$

Considering stationary frame of reference (i.e., $\omega = 0$), (15) and (16) can be reframed as

$$\psi_{\alpha s} = \int (\upsilon_{\alpha s} - i_\alpha R_s)dt \tag{17}$$

$$\psi_{\beta s} = \int (\upsilon_{\beta s} - i_\beta R_s)dt. \tag{18}$$

Using (17) and (18), the magnitude and angle of stator flux is given by

$$|\psi_s| = \sqrt{\left(\psi_{\alpha s}^2 + \psi_{\beta s}^2\right)} \tag{19}$$

$$\rho = \tan^{-1}\left(\frac{\psi_{\beta s}}{\psi_{\alpha s}}\right). \tag{20}$$

The torque equation in terms of $\alpha - \beta$ is shown in the following equation:

$$\overline{T_e} = \frac{2}{3}\left(\frac{P}{2}\right)(\psi_{\alpha s} i_{\beta s} - \psi_{\beta s} i_{\alpha s}). \tag{21}$$

The mathematical implementation of stator flux, stator flux angle, and torque is represented in the block diagram shown in Fig. 7, and the stator flux angle is used to identify the sector angle. In this paper, the total sectors are chosen as 12 and each sector has a width of 30°.

The command stator flux (ψ_s^*) and torque (T_e^*) magnitudes are compared with the respective estimated values of the flux (19) and torque (21). The errors are determined by using flux control loop and the torque control loop (see Fig. 6), respectively.

The flux-loop controller has two levels of digital output according to the following relations:

$$H_\psi = 1 \quad \text{For } E_\psi \geq +HB_\psi$$

$$H_\psi = -1 \quad \text{For } E_\psi < -HB_\psi$$

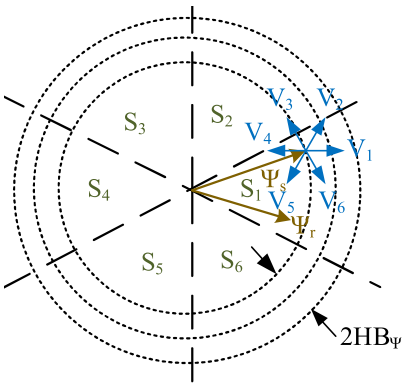

Fig. 8. Trajectory of stator flux vector in DTC control.

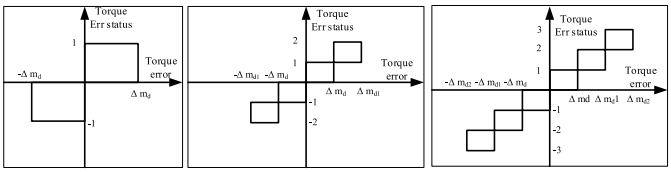

Fig. 9. THBCs: 3L (left), 5L (middle), and 7L (right).

where H_ψ = flux status and $2HB_\psi$ = total hysteresis-bandwidth controller of stator flux. The circular trajectory of the command flux vector ψ_s^* with the hysteresis band rotates in an anticlockwise direction is shown in Fig. 8.

As stated earlier, three different THBC are considered in this paper with 3L, 5L, and 7L, respectively, as shown in Fig. 9. The performance of DTC for OEWIMD is evaluated with these three controllers.

The digital outputs of the THBC, as per the number of levels, are given as follows.

A. 3L-THBC

$$\begin{aligned}
&H_{T_e} = +1 \quad \text{for } \Delta m_d > +HB_{T_e}\\
&H_{T_e} = 0 \quad \text{for } -HB_{T_e} < \Delta m_d < +HB_{T_e}\\
&H_{T_e} = -1 \quad \text{for } \Delta m_d < -HB_{T_e}
\end{aligned}$$

where H_{T_e} is torque status and HB_{T_e} = total hysteresis-bandwidth controller of torque. The 3L-THBC can achieve 2Ls as well as 3Ls in motor phase voltages. For the 2L operation smaller vectors are switched, while medium and large vectors are switched to obtain the 3L operation.

B. 5L-THBC

$$\begin{aligned}
&H_{T_e} = +2 \quad \text{for } \Delta m_{d1} > +HB_{T_e}\\
&H_{T_e} = +1 \quad \text{for } 0.5HB_{T_e} < \Delta m_{d1} < +HB_{T_e}\\
&H_{T_e} = 0 \quad \text{for } -0.5HB_{T_e} < \Delta m_d < +0.5HB_{T_e}\\
&H_{T_e} = -1 \quad \text{for } -0.5HB_{T_e} < -\Delta m_{d1} < -HB_{T_e}\\
&H_{T_e} = -2 \quad \text{for } -\Delta m_{d1} < -HB_{T_e}.
\end{aligned}$$

Whenever the output of the 5L-THBC is "±2," the large and middle vectors are switched. If its output is "±1," then the smaller vectors are switched.

TABLE II
SWITCHING TABLE FOR 3L OEWIMD DTC WITH 3L-THBC

Sector Number	$H_\psi = 1$			$H_\psi = -1$			Speed (RPM)
	H_{T_e}			H_{T_e}			
	1	0	-1	1	0	-1	
S_1	L_2	N	M_5	M_2	N	L_5	$\|V\| < 600$ & $\|V\| > 600$
S_2	M_2	N	L_6	L_3	N	M_5	
S_3	L_3	N	M_6	M_3	N	L_6	
S_4	M_3	N	L_1	L_4	N	M_6	
S_5	L_4	N	M_1	M_4	N	L_1	
S_6	M_4	N	L_2	L_5	N	M_1	
S_7	L_5	N	M_2	M_5	N	L_2	
S_8	M_5	N	L_3	L_6	N	M_2	
S_9	L_6	N	M_3	M_6	N	L_3	
S_{10}	M_6	N	L_4	L_1	N	M_3	
S_{11}	L_1	N	M_4	M_1	N	L_4	
S_{12}	M_1	N	L_5	L_2	N	M_4	
S_1	S_2	N	S_6	S_3	N	S_5	$\|V\| < 600$ & $\|V\| > 600$
S_2	S_2	N	S_6	S_3	N	S_5	
S_3	S_3	N	S_1	S_4	N	S_6	
S_4	S_3	N	S_1	S_4	N	S_6	
S_5	S_4	N	S_2	S_5	N	S_1	
S_6	S_4	N	S_2	S_5	N	S_1	
S_7	S_5	N	S_3	S_6	N	S_2	
S_8	S_5	N	S_3	S_6	N	S_2	
S_9	S_6	N	S_4	S_1	N	S_3	
S_{10}	S_6	N	S_4	S_1	N	S_3	
S_{11}	S_1	N	S_5	S_2	N	S_4	
S_{12}	S_1	N	S_5	S_2	N	S_4	

C. 7L-THBC

$$\begin{aligned}
&H_{T_e} = +3 \quad \text{for } \Delta m_{d2} > +0.7HB_{T_e}\\
&H_{T_e} = +2 \quad \text{for } 0.6HB_{T_e} < \Delta m_{d2} < +0.7HB_{T_e}\\
&H_{T_e} = +1 \quad \text{for } 0.3HB_{T_e} < \Delta m_{d1} < +0.6HB_{T_e}\\
&H_{T_e} = 0 \quad \text{for } -0.3HB_{T_e} < \Delta m_d < +0.3HB_{T_e}\\
&H_{T_e} = -1 \quad \text{for } -0.3HB_{T_e} < -\Delta m_{d1} < -0.6HB_{T_e}\\
&H_{T_e} = -2 \quad \text{for } -0.6HB_{T_e} < -\Delta m_{d2} < -0.7HB_{T_e}\\
&H_{T_e} = -3 \quad \text{for } -\Delta m_{d2} < -0.7HB_{T_e}.
\end{aligned}$$

In this case, the torque controller possesses 7Ls of digital output based on the error in torque. When the output of the THBC is "±3," the error in torque is very high and hence larger vectors are switched. If the output is "±2," the error in torque is medium and hence medium vectors are switched. Smaller vectors are switched when the output is "±1," i.e., the error in torque is low.

The status of the flux hysteresis band controller (FHBC), THBC, and stator flux angle will decide, whether flux and torque are to be decreased or increased. Based on the signals of the FHBC and THBC, appropriate voltage vectors are selected from the look-up tables, presented in Tables II–IV, respectively.

The increment or decrement of flux and torque for the OEWIMD based on the selection of voltage space vector of the dual-inverter system over the 12 sectors for sinusoidal stator flux can be easily visualized in Fig. 10.

The circle represents the trajectory of sinusoidal flux and the hexagons mounted on the circumference of the circle show the voltage vectors available at various sampling instants. For the particular instant shown in Fig. 10, wherein the tip of

TABLE III
SWITCHING TABLE FOR 3L OEWIMD DTC WITH 5L-THBC

Sector Number	$H_\psi = 1$					$H_\psi = -1$				
	H_{T_e}					H_{T_e}				
	2	1	0	-1	-2	2	1	0	-1	-2
S_1	L_2	S_2	N	S_6	M_5	M_2	S_3	N	S_5	L_5
S_2	M_2	S_2	N	S_6	L_6	L_3	S_3	N	S_5	M_5
S_3	L_3	S_3	N	S_1	M_6	M_3	S_4	N	S_6	L_6
S_4	M_3	S_3	N	S_1	L_1	L_4	S_4	N	S_6	M_6
S_5	L_4	S_4	N	S_2	M_1	M_4	S_5	N	S_1	L_1
S_6	M_4	S_4	N	S_2	L_2	L_5	S_5	N	S_1	M_1
S_7	L_5	S_5	N	S_3	M_2	M_5	S_6	N	S_2	L_2
S_8	M_5	S_5	N	S_3	L_3	L_6	S_6	N	S_2	M_2
S_9	L_6	S_6	N	S_4	M_3	M_6	S_1	N	S_3	L_3
S_{10}	M_6	S_6	N	S_4	L_4	L_1	S_1	N	S_3	M_3
S_{11}	L_1	S_1	N	S_5	M_4	M_1	S_2	N	S_4	L_4
S_{12}	M_1	S_1	N	S_5	L_5	L_2	S_2	N	S_4	M_4

TABLE IV
SWITCHING TABLE FOR 3L OEWIMD DTC WITH 7L-THBC

H_ψ	H_{T_e}	Sector Number											
		S_1	S_2	S_3	S_4	S_5	S_6	S_7	S_8	S_9	S_{10}	S_{11}	S_{12}
1	3	L_2	L_2	L_3	L_3	L_4	L_4	L_5	L_5	L_6	L_6	L_1	L_1
	2	M_1	M_2	M_2	M_3	M_3	M_4	M_4	M_5	M_5	M_6	M_6	M_1
	1	S_2	S_2	S_3	S_3	S_4	S_4	S_5	S_5	S_6	S_6	S_1	S_1
	0	N	N	N	N	N	N	N	N	N	N	N	N
	-1	S_6	S_6	S_1	S_1	S_2	S_2	S_3	S_3	S_4	S_4	S_5	S_5
	-2	M_5	M_6	M_6	M_1	M_1	M_2	M_2	M_3	M_3	M_4	M_4	M_5
	-3	L_6	L_6	L_1	L_1	L_2	L_2	L_3	L_3	L_4	L_4	L_5	L_5
-1	3	L_3	L_3	L_4	L_4	L_5	L_5	L_6	L_6	L_1	L_1	L_2	L_2
	2	M_2	M_3	M_3	M_4	M_4	M_5	M_5	M_6	M_6	M_1	M_1	M_2
	1	S_3	S_3	S_4	S_4	S_5	S_5	S_6	S_6	S_1	S_1	S_2	S_2
	0	N	N	N	N	N	N	N	N	N	N	N	N
	-1	S_5	S_5	S_6	S_6	S_1	S_1	S_2	S_2	S_3	S_3	S_4	S_4
	-2	M_4	M_5	M_5	M_6	M_6	M_1	M_1	M_2	M_2	M_3	M3	M_4
	-3	L_5	L_5	L_6	L_6	L_1	L_1	L_2	L_2	L_3	L_3	L_4	L_4

the stator flux vector is situated in sector II, the flux status is " −1" and torque status positive (either of "1," "2," and "3"). It can easily be identified from Table IV that for the present situation, the available vectors are L_3, M_3, and S_3. Three lines represent the three possible flux vectors. It is clearly observable that all of three vectors are capable of decreasing the flux. If S_3 is applied, change in angle ($\Delta\gamma$) will be least and if L_3 is applied it will be maximum. Hence, if the torque error status is equal to "3," L_3 should be applied; for the torque error status "2," M_3 should be applied; for torque error status "1," S_3 should be applied. Similarly, the others three instants can also be verified.

V. PREDICTIVE TORQUE CONTROL STRATEGY FOR THREE-LEVEL OEWIMD

In recent times, the potential of the PTC has extensively been explored for the motor drive applications. In this paper, the conventional PTC technique is implemented for the 3L OEWIMD topology (shown in Fig. 1). The performance of the PTC and the DTC techniques are then compared. The block diagram for the implementation of PTC for 3-L OEWIMD is shown in Fig. 11.

From the block diagram (Fig. 11), it can be observed that from the measured stator currents (i_{as}, i_{bs}), the dc-link voltage (V_{DC}), and the motor parameters (see Table V), the stator

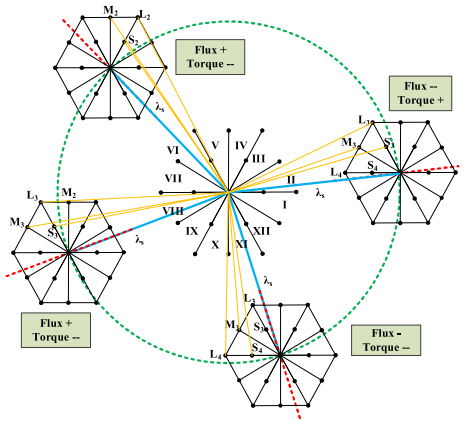

Fig. 10. Selection of suitable voltage space vector for dual-inverter system.

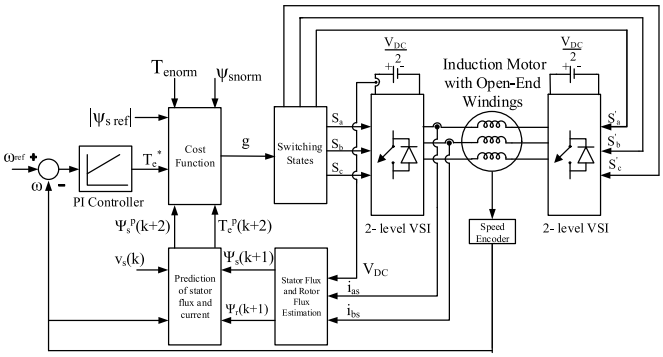

Fig. 11. Block diagram of PTC for 3L OEWIMD.

flux (ψ_s) and the rotor flux (ψ_r) are estimated, at the present sampling step (T_s) using forward Euler's approximation [24] as

$$\psi_s(k) = \psi_s(k-1) + T_s V_s(k) - R_s T_s i_s(k) \quad (22)$$

$$\psi_r(k) = \frac{L_r}{L_m}\psi_s(k) + i_s(k)\left(L_m - \frac{L_r L_s}{L_m}\right) \quad (23)$$

where $V_s(k)$ is the dual-inverter voltage. In the case of PTC, the stator flux and the electromagnetic torque (T_e) are predicted at the $(k+1)$th sampling instant from the estimated values of $\psi_s(k)$ and $\psi_r(k)$. The predicted stator flux expression is given by

$$\psi_s^p(k+1) = \psi_s(k) + T_s V_s(k) - R_s T_s i_s(k). \quad (24)$$

From (12), to predictive T_e, it is needed to predict the stator current i_s at the instant $(k+1)$, which is given in the following equation [24]:

$$i_s^p(k+1) = \left(1 + \frac{T_s}{\tau_\sigma}\right) i_s(k) + \frac{T_s}{\tau_\sigma + T_s} \times \left\{\frac{1}{R_\sigma}\left[\left(\frac{k_r}{\tau_r} - k_r j\omega_m\right)\psi_r(k) + V_s(k)\right]\right\} \quad (25)$$

where $T_s = L_s/R_s, T_r = L_r/R_{rp}, \sigma = 1 - (((L_m)^2)/(L_r L_s)), k_r = L_m/L_r, R_\sigma = R_s + K_r^2 R_{rp}$, and $\tau_\sigma = \sigma L_s/R_\sigma$.

Owing to the problem of sampling delay [24], the prediction of stator flux and stator current are done at the $(k+2)$th owing

TABLE V
SPECIFICATIONS OF SEMICONDUCTOR DEVICES AND EXPERIMENTAL PARAMETERS OF THE 3L OEWIMD

DC-Link Voltage		300 V
Rated Speed of the OEWIMD		800 RPM
Reference flux $(\psi_{s_{norm}})$		1 Wb
Band of Flux hysteresis window		$\pm$0.001Wb
Stator Resistance of OEWIMD (R_s)		1.5 Ω
Rotor Resistance of OEWIMD (R_r')		2.1 Ω
Stator inductance of OEWIMD(L_s)		0.5632 H
Rotor inductance of OEWIMD(L_r')		0.5632 H
Magnetizing inductance of OEWIMD (L_m)		0.54 H
Rated torque of OEWIMD $(T_{e_{norm}})$		25 N-m
Band of Torque hysteresis window	DTC with 3-level OEWIM (3L and 5L-THBCs)	$\pm$1
	DTC with 3-level OEWIM (7L-THBC)	$\pm$0.7
PI controller values (3L, 5L & 7L-THBCs)		$k_p = 0.4$ $k_i = 0.15$
PI controller values (PTC)		$k_p = 1$ $k_i = 0.25$
Semikron IGBT switch		1200 V, 30A
Driver IC (A3120)		15V, 2.5 A

to this maneuver; (24) and (25) are get transformed as

$$\psi_s^p(k+2) = \psi_s(k+1) + T_s V_s(k+1) - R_s T_s i_s(k+1) \tag{26}$$

$$i_s^p(k+2) = \left(1 + \frac{T_s}{\tau_\sigma}\right) i_s(k+1) + \frac{T_s}{\tau_\sigma + T_s} \times \left\{\frac{1}{R_\sigma}\left[\left(\frac{k_r}{\tau_r} - k_r j\omega_m\right)\psi_r(k+1) + V_s(k+1)\right]\right\}. \tag{27}$$

From (26) and (27), the predicted T_e at the instant $(k+2)$ is given as

$$T_e^p(k+2) = \frac{2}{3}\frac{P}{2}\mathrm{Im}\left\{\overline{\psi}_s^p(k+2) i_s^p(k+2)\right\} \tag{28}$$

where P is the number of poles and $\overline{\psi}_s^p$ is the complex conjugate of ψ_s^p.

From (26)–(28), it can be observed that the predicted values are dependent on the dual-inverter voltage of the OEWIMD $V_s(k)$. As explained earlier, the 3L OEWIMD possesses a total of 64 space vector combinations spread over 19 space vector locations. Using (9)–(11), the voltage space vector $[V_s(K)]$ is computed in stationary frame of reference for all of the 19 switching space vector combinations.

Finally, the switching state selection is made by the cost function, based on the comparison between the reference torque (output of speed PI controller T_e^*) and the reference flux ($\psi_{s_{\mathrm{ref}}} = 1\ wb$) with the predicted values, given in (26) and (28). In one sampling time period, the cost function is evaluated for all of the 19 space vector combinations. The optimal switching vector is then selected based on the minimal values of errors in the respective reference and predicted values. The control signals (i.e., gating signals) for the dual-inverter system are then generated based on the selected voltage vector.

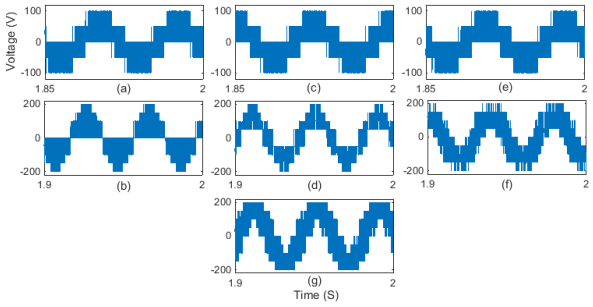

Fig. 12. Simulated phase voltages for 3L OEWIMD at a speed of (a), (c), and (e) 400 RPM and (b), (d), (f) and (g) 750 RPM. DTC: (a) and (b) 3L-THBC; (c) and (d) 5L-THBC; and (e) and (f) 7L-THBC. (g) PTC.

The cost function is defined as

$$g_i = \left|T_e^* - T_e^p(k+2)_i\right| + \lambda_\psi \left|\psi_{s_{\mathrm{ref}}} - \psi_s^p(k+2)_i\right| \tag{29}$$

where $i \in [0, 1, \ldots, 18]$ and λ_ψ denotes the weight factor, which increases or decreases the relative importance of the torque versus flux control. The tuning of λ_ψ is often a cumbersome process. However, the normalized cost function, wherein each term is divided by its rated value [26] could considerably simplifying the formulation of the cost function. Based on this method, the cost function is modified as

$$g_i = \frac{\left|\left(T_e^* - T_e^p(k+2)_i\right)^2\right|}{T_{e_{\mathrm{norm}}}^2} + \lambda_\psi \frac{\left|\left(\psi_{s_{\mathrm{ref}}} - \psi_s^p(k+2)_i\right)^2\right|}{|\psi_{s_{\mathrm{norm}}}|^2} \tag{30}$$

where $T_{e_{\mathrm{norm}}}$ and $\psi_{s_{\mathrm{norm}}}$ are the rated torque and the stator flux values of the OEWIMD. Employment of this cost function with $\lambda_\psi = 1$ would ensure that the same importance is given to both torque and stator flux terms.

VI. SIMULATION AND EXPERIMENTAL RESULTS

The relative performance of the three THBCs and PTC technique is assessed with the aid of simulation studies, which is verified by experimentation. The block diagram shown in Figs. 6 and 11 was implemented by using MATLAB/Simulink software. A 5-HP, 400-V (line–line, rms), 50-Hz, three-phase OEWIM drive ($R_s = 4.215\ \Omega$; $R_{r'} = 4.185\ \Omega$; $x_{ls} = x_{lr'} = 5.502\ \Omega$; $X_m = 162.3\ \Omega$; $J = 0.0131\ \mathrm{Kg-m^2}$; $B = 0.002985\ \mathrm{N \cdot m \cdot s}$; $P = 4$) is chosen for simulation. The total dc-link voltage for dual inverter system was chosen as 300 V (i.e., each inverter operates with a dc-link voltage of 150 V). To facilitate a fair comparison, the same flux controller (which is a 2L hysteresis controller) and flux reference is employed for all of the three THBCs as well as for the PTC.

The simulated motor phase voltages are shown in Fig. 12, wherefrom it is evident that the motor phase voltage resembles that of the output of a 2L VSI at lower speeds (400 RPM), while it displays the 3L waveform at higher speeds (750 RPM) in the case of DTC. In PTC, the voltage waveform displays three levels, only at higher speeds.

The simulated steady-state motor phase currents are shown in Fig.13, for DTC with the conventional drive, OEWIMD, when THBC possesses 3Ls, 5Ls, and 7Ls and the PTC with OEWIMD. It is evident from these plots that there is

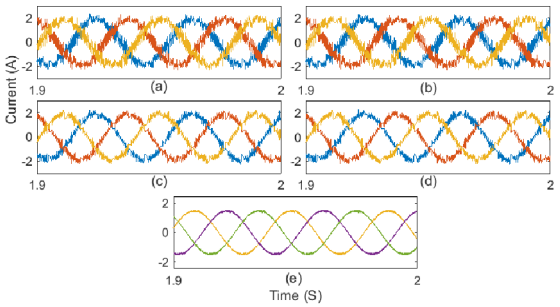

Fig. 13. Simulated motor steady state phase currents: (a) 2L DTC, (b)–(d) 3L OEWIMD DTC with 3L-, 5L-, 7L-THBCs, respectively, and (e) 3L OEWIMD with PTC.

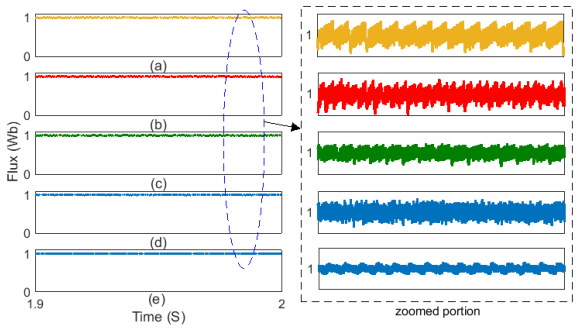

Fig. 14. Simulated stator flux with zoomed-in portion: (a) 2L DTC, 3L OEWIMD DTC, (b) 3L-THBC (c) 5L-THBC (d) 7L-THBC, and (e) PTC with 3L OEWIMD.

a considerable reduction in the ripple in the motor phase current with the OEWIMD compared to the conventional DTC drive. Also, the ripple with 5L- and the 7L-THBCs is smaller compared to the 3L-THBC. It is evident from Fig. 13(a)–(e) that the ripple in motor phase current with PTC has the least ripple compared to all of the DTC variants.

Fig. 14 shows the simulation results of motor steady-state stator flux for DTC with conventional drive, OEWIMD, when THBC having 3L, 5L, 7L, and the PTC with OEWIMD. These plots confirm that that the flux remains essentially the same (in terms of both the average value). Here also, the PTC registers a better performance, closely followed by the 5L-THBC.

Fig. 15 shows the simulated motor steady state torque. It can be observed that the torque ripple is reduced with 3L OEWIMD. In particular, the torque ripple with 5L-THBC, 7L-THBC, and PTC is considerably lower compared to the conventional drive and the OEWIMD with 3L-THBC.

For the experimental verification of a 3L OEWIMD (3.7 KW, 415 V, 7.5 A, 1445 RPM, 50 Hz, 4-pole, 3-Ø supply), a prototype was built in the laboratory. The control signals for the dual-inverter system are generated by using the dSPACE 1104 controller. One Hall-effect voltage sensor, two Hall-effect current sensors, and one speed encoder are, respectively, employed for the measurement of the dc-link voltage, two phase currents, and the speed, respectively. All these measurements are instrumental for the estimation of instantaneous flux and torque of the OEWIMD. The rated

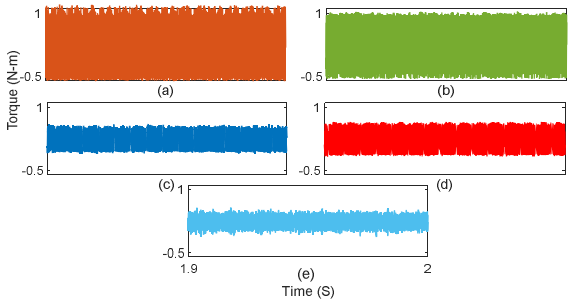

Fig. 15. Simulated motor steady-state torque: (a) 2L DTC, 3L OEWIMD DTC, (b) 3L-THBC, (c) 5L-THBC, (d) 7L-THBC, and (e) PTC with 3L OEWIMD.

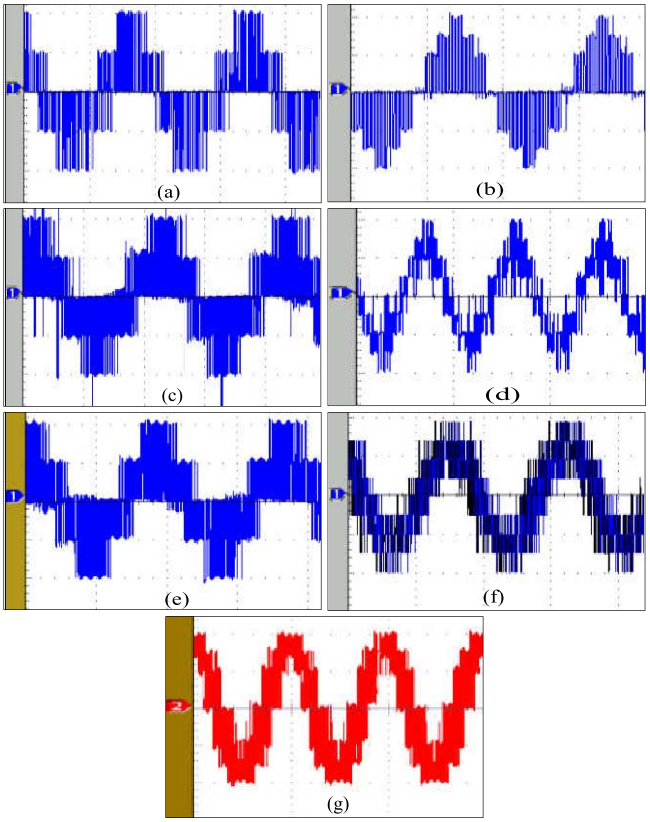

Fig. 16. Phase voltages of OEWIMD at a speed of (a), (c), and (e) 400 and (b), (d), (f), and (g) 750 RPM. (a) and (b) 3L-THBC. (c) and (d) 5L-THBC. (e) and (f) 7L-THBC-based DTC. (g) PTC. Scale: X-axis: 40 ms/div. Y-axis: (a), (c), and (e) 50 V/div and (b), (d), (f), and (g) 100 V/div.

phase voltage that can be applied to motor is 230 V (rms), corresponding to the dc-link voltage of 564 V. However, in the present experimental study (for 2L DTC, 3L OEWIMD DTC, and 3L OEWIMD PTC), the dc-link voltage is restricted to 300 V. From the above discussion, it is evident that, the rated speed of 1500 RPM corresponds to the dc-link voltage of 564 V (which corresponds to 800 RPM for a voltage of 300 V). The other operational parameters and specifications of switching devices are enumerated in Table V.

Fig. 16 shows experimentally obtained phase voltages for DTC with 3L open-end winding induction motor with three torque hysteresis controller and PTC with 3L OEWIM. As explained earlier, and is evident from Fig. 16 that the

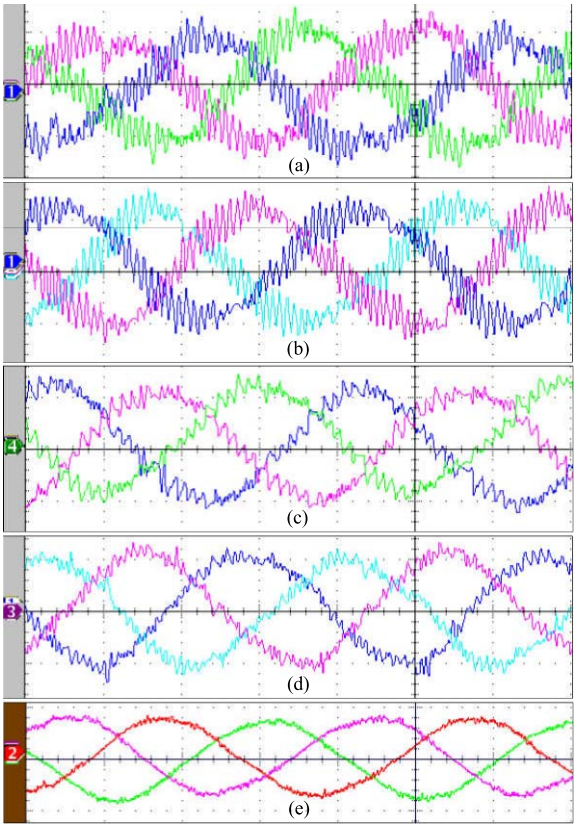

Fig. 17. Steady-state phase currents. (a) 2L DTC, (b)–(d) 3L OEWIMD with 3L, 5L, and 7L-THBCs, respectively, (e) 3L OEWIMD with PTC. Scale: X-axis: 10 ms/div; Y-axis: 1 A/div.

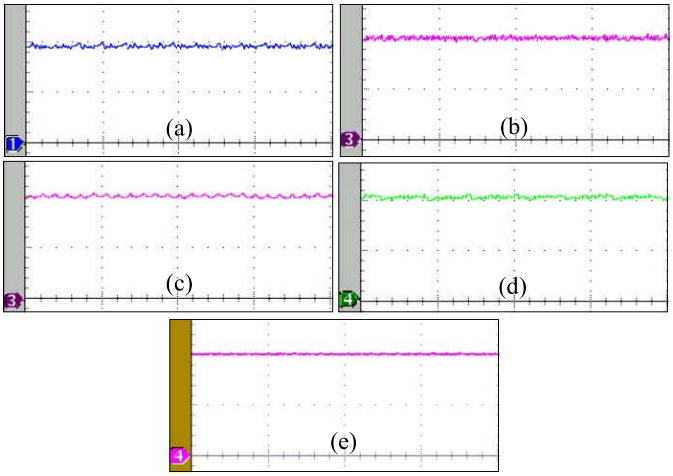

Fig. 18. Steady-state stator flux. (a) 2L DTC, (b)–(d) 3L OEWIMD using 3L-THBC-, 5L-THBC, and 7L-THBC-based DTC, (e) 3L OEWIMD with PTC. Scale: X-axis: 20 mS/div; Y-axis: 0.5 Wb/div.

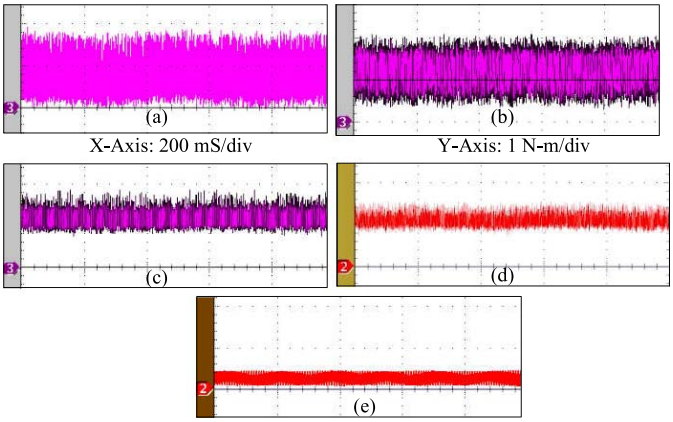

Fig. 19. Steady-state torque ripple at 750 RPM. (a) 2L DTC, (b)–(d) DTC with 3L OEWIMD using 3L-, 5L-, and 7L-THBCs, respectively, and (e) PTC with 3L OEWIMD.

3L OEWIMD DTC strategy runs the drive as 2L inverter in the lower range of speeds and reduces the switching losses.

The experimentally obtained steady-state no-load three-phase stator currents with the classical DTC with 2L VSI and 3L OEWIMD DTC and with 3L OEWIMD PTC are shown in Fig. 17. It is evident that the ripple in the motor phase current with the 3L OEWIM employing the three torque hysteresis controllers is considerably lower compared to the 2L conventional DTC drive. Among the 3L OEWIMD control strategies, the PTC technique registers lesser ripple in the motor phase current at no load. These experimental results are in agreement with the simulation results shown in Fig. 13.

Fig. 18 shows the experimentally obtained estimated stator flux. It can be observed that the flux ripple is slightly lesser with all of the DTC- and PTC-driven OEWIMD compared to the conventional drive.

Fig. 19 shows steady-state torque ripple at 750 RPM for DTC with conventional drive, DTC with 3L OEWIMD using 3L-, 5L-, and 7L-THBCs and PTC with 3L OEWIMD. It can be concluded that torque ripple in 3L OEWIM with DTC and PTC is effectively reduced compared to that in DTC with 2L VSI which represents the smooth operation of motor drive. Among the proposed three THBCs and the PTC, the 7L-THBC-based DTC and PTC with 3L OEWIMD show lesser torque ripple. Thus, the 7L-THBC and the PTC result in lesser bearing stresses.

The experimental results presented in Fig. 16 convincingly show that the quality of the voltage waveform is enhanced as the number of levels in the THBC is increased. Besides decreasing the THD in the voltage waveform, the number of levels in THBC reduces the current ripple (Fig. 17) and torque ripple (Fig. 19). While the decreased dv/dt and the THD in voltage result in the reduction of stress on the insulation of the motor, the decreased torque ripple would result in the reduction wear and tear of the motor bearings. This justifies the increase in the number of levels in the THBC. It should also be noted that number of levels are increased simply by using a modified lookup table to output appropriate voltage vectors. It is also evident that the PTC performs slightly better compared to the 5L-THBC- and 7L-THBC-based DTC in terms of the current and flux ripple. However, the performance of 7L-THBC and the PTC is almost similar so far as the torque ripple is concerned. However, the PTC results in an increased computational burden on the controller. While the structural implementation of 3L OEWIMD DTC mainly depends on the accuracy of stator resistance, the 3L OEWIMD PTC depends on all of the motor parameters.

The experimentally obtained phase current, stator flux, rotor speed, and electromagnetic torque of the conventional 2L DTC, THBC-based 3L OEWIMD DTC, and 3L OEWIMD

PTC techniques at a low speed of 90 RPM (i.e., at a supply frequency of 3 Hz) are presented in Fig. 20.

From Fig. 20, it can be observed that at low speeds, the performance of the 5L-THBC-based DTC for the OEWIMD is better compared to the other two THBC techniques, as the fluctuations in motor torque as well as in the rotor speed are small. It may also be noted the 5L-THBC-based DTC drive performs on par to the PTC in terms of current, flux, and speed.

These experimental results demonstrate the effectiveness of the employment of multilevel (i.e., 3L, 5L, and 7L) THBCs for the DTC-controlled 3L OEWIMD and the PTC-controlled 3L OEWIMD.

VII. Performance Evaluation of Three-Level OEWIMD

In order to facilitate a relative comparison of the 3L-, 5L-, and 7L-THBCs, and the 3L- OEWIMD PTC, the conventional DTC with the 2L VSI is taken as the benchmark. The performance of the OEWIMD is compared with this benchmark in terms of flux ripple, torque ripple, and total power loss in the dual-inverter system and THD in no-load current. For the rest of this paper, the conventional DTC-controlled 2L VSI-driven induction motor is referred as the conventional DTC drive.

In order to make a fair comparison to calculate the power loss, the total dc-link voltage is chosen as 564 V. A load of 20 N·m (approximately 80% of the full load) is applied on the motor shaft, to compute the inverter losses. To compute the inverter loss an improvized loss model, which was proposed in [33] and [35] for loss calculation of 4L OEWIMD. The same model was extended here to compute the losses for the 2L VSI fed DTC Induction motor as well as for the 3L OEWIMD.

The total power loss in the dual-inverter system (P_{DI}) comprises of the switching loss (P_{SW}) in power semiconductor devices and the conduction loss (P_{Con}) in them.

The switching power loss (P_{SW}) is the sum of the $P_{\mathrm{SW,ON}}$ and $P_{\mathrm{SW,OFF}}$, where $P_{\mathrm{SW,ON}}$ is the switching loss during the turn-ON period of the switch and $P_{\mathrm{SW,OFF}}$ is the switching loss during the turn-OFF period of the switching device. P_{SW} and P_{Con} are measured by extracting the simulation data of the voltage across the switch (v_{SW}) and the current through the switch (i_{ON}). The expression for P_{SW} is given as [36]

$$P_{\mathrm{SW}} = \left[\frac{1}{2} v_{\mathrm{SW}} i_{\mathrm{SW}} \left(t_{\mathrm{SWON}} + t_{\mathrm{SWOFF}}\right)\right] \times f_S$$

$$P_{\mathrm{SW}} = \left[\frac{1}{2} v_{\mathrm{SW}} i_{\mathrm{SW}} (t_{ri} + t_{fv}) + \frac{1}{2} v_{\mathrm{SW}} i_{\mathrm{SW}} (t_{rv} + t_{fi})\right] \times f_s \tag{31}$$

$$P_{\mathrm{Con}} = \frac{V_{\mathrm{ON}} I_{\mathrm{ON}} t_{\mathrm{ON}}}{T_S}. \tag{32}$$

The following data are assumed to compute the switching and conduction loss in each device: $t_{fv} = 1\ \mu$s, $t_{rv} = 2\ \mu$s, $t_{fi} = 4\ \mu$s, $t_{ri} = 2\ \mu$s, and $v_{\mathrm{ON}} = 1$ V.

Fig. 21 shows the total dual-inverter loss (i.e., sum of the switching loss and conduction loss) for the 3L OEWIMD with different THBCs, PTC, and the conventional 2L DTC, for varying speed from 300 to 1500 RPM and is shown as

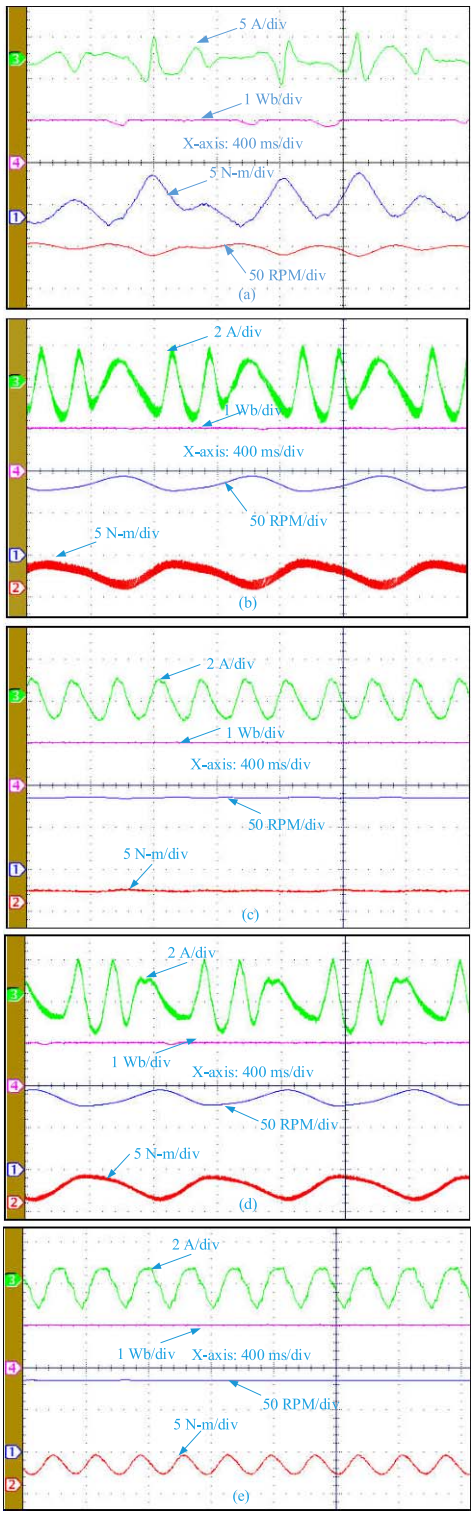

Fig. 20. Experimental results at a speed of 90 RPM. (a) 2L DTC, (b)–(d) 3L OEWIMD using 3L-THBC-, 5L-THBC-, and 7L-THBC-based DTC, (e) 3L OEWIMD with PTC.

per unit on the X-axis. It can be observed that compared to the 2L DTC, the 3L OEWIMD with the proposed THBCs perform well. All the three THBCs register almost similar total dual-inverter loss up to the speed of 900 RPM. Above this speed, the 5L-THBC displays a better performance. Among the DTC and PTC of 3L OEWIMD, the dual inverter loss for PTC is higher compared to the THBC-based DTC.

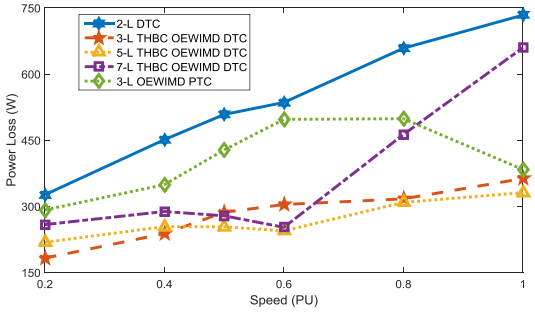

Fig. 21. Total power loss in the dual-inverter system.

TABLE VI
SWITCHING AND CONDUCTION LOSS

Speed (PU)		0.2	0.4	0.5	0.6	0.8	1
2-L DTC	P_{SW} (W)	312.49	437.73	494.99	522.26	645.56	720.82
	P_{Con} (W)	13.72	13.44	13.31	13.24	12.96	12.86
	P_{DI} (W)	326.21	451.17	508.3	535.5	658.52	733.68
3-L THBC OEWIMD DTC	P_{SW} (W)	154.12	209.91	258.59	276.30	289.12	335.04
	P_{Con} (W)	28.31	28.08	27.81	27.71	27.76	27.90
	P_{DI} (W)	182.43	237.99	286.4	304.01	316.88	362.94
5-L THBC OEWIMD DTC	P_{SW} (W)	190.47	225.92	225.66	216.10	281.06	303.08
	P_{Con} (W)	27.96	27.87	27.92	28.07	27.80	27.86
	P_{DI} (W)	218.43	253.79	253.58	244.17	308.86	330.94
7-L THBC OEWIMD DTC	P_{SW} (W)	230.70	260.57	250.71	224.36	435.95	634.15
	P_{Con} (W)	27.78	27.59	27.75	27.99	26.89	25.83
	P_{DI} (W)	258.48	288.16	278.46	252.35	462.84	659.98
OEWIMD PTC	P_{SW} (W)	282.75	338.67	417.26	485.44	485.80	368.31
	P_{Con} (W)	8.92	10.56	10.63	11.77	12.85	14.98
	P_{DI} (W)	291.67	349.23	427.89	497.21	498.65	383.29

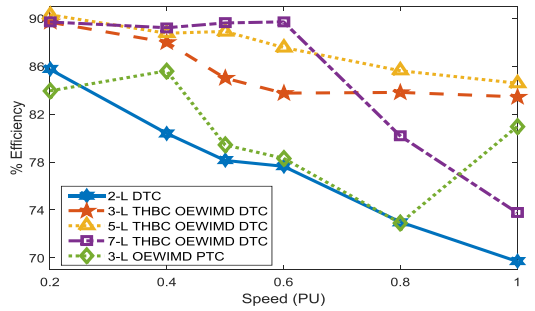

Fig. 22. Efficiency of the dual-inverter system.

The numerical information of the switching and conduction losses of the conventional as well as the proposed techniques is given in Table VI.

The overall efficiency of the dual-inverter system of the OEWIMD based on DTC, PTC, and for conventional DTC is presented in Fig. 22. The total power loss in the dual-inverter

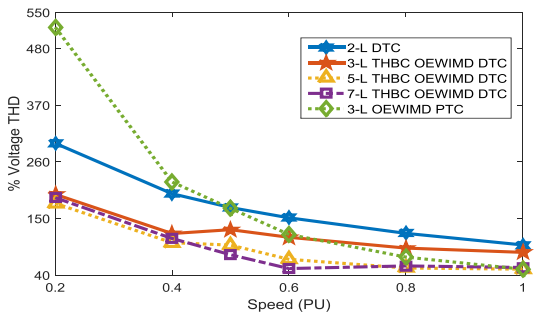

Fig. 23. Voltage THD.

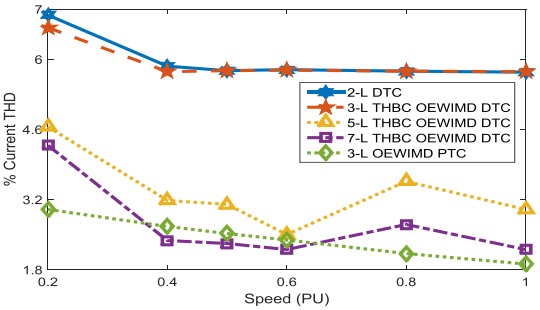

Fig. 24. No-load current THD.

system is the sum of the conduction loss and the switching loss given in (31) and (32). The input power to the dual-inverter system is obtained by doubling the input power (i.e., the dc-side power) of one inverter. The instantaneous input dc-current (i_{DC}) for one inverter (say inverter 1, Fig. 1) is obtained with the help of the following equation:

$$i_{DC} = S_a i_{as} + S_b i_{bs} + S_c i_{cs} \tag{33}$$

where S_a, S_b, and S_c are the gating pulses to inverter 1, i_{as}, i_{bs}, and i_{cs} are the Phase currents of OEWIMD.

The rms current is then obtained for one cycle of the fundamental component of the motor phase currents. With the knowledge of this rms current and the total dual-inverter power loss, it is possible to estimate the efficiency of the dual-inverter system. It can be observed that the THBC-based DTC techniques are results in high converter efficiency compared to the conventional DTC and PTC with 3L OEWIMD.

The other performance indices considered are THD in voltage, no-load current THD are shown in Figs. 23 and 24, respectively. Based on Figs. 23 and 24, it can be concluded that all of the proposed THBC-based OEWIMD DTC techniques outperform the 2L DTC. Among the proposed three DTC techniques and PTC for the OEWIMD, the 7L-THBC-based technique performs better in terms of voltage THD, whereas in the case of current THD, the PTC performs better compared to other techniques in low- and high-speed regions.

The DTC strategies for the OEWIMD employ hysteresis controllers, as well as the PTC strategy result in variable switching frequency. Table VII presents the details regarding the computational burden on the controller for all of the control strategies. The computational burden incurred at various stages of implementation is also presented in Table VII. The time

TABLE VII
ALGORITHM EXECUTION TIMES WITH SAMPLING TIME (T_S) = 80 μS

Time (μS)	2-L DTC	3-L THBC OEWIMD DTC	5-L THBC OEWIMD DTC	7-L THBC OEWIMD DTC	OEWIMD PTC
t_{meas}	7.94	7.94	7.94	7.94	7.94
t_{con}	7.01	4.89	4.37	6.11	3.16
$t_{est-DTC}$	29.39	27.65	27.64	27.65	-
$t_{est-PTC}$	-	-	-	-	52.11
Total	44.35	40.48	39.95	41.7	63.21

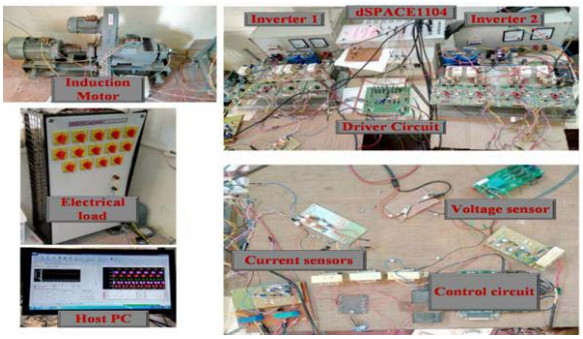

Fig. 25. Experimental setup.

needed to measure the phase currents, speed and dc-link voltage for the OEWIMD is represented with t_{meas}. The reference generation, speed control, and hysteresis band controllers execution time is represented with t_{con}. The symbol $t_{\text{est}-\text{DTC}}$ represents the total execution time needed for the estimation of torque and flux and the switching vector selection from the lookup table in the case of the 2L DTC and THBC-DTC scheme. Similarly, the time needed for the estimation, delay compensation, optimization, and selection of switching vector for the PTC-based OEWIMD is represented with $t_{\text{est}-\text{PTC}}$.

From Table VII, it can be conclude that the overall computational burden is less for the 5L THBC-based DTC compared to the other control strategies.

Figs. 18–24 show the comparative performance among the conventional DTC drive and the 3L OEWIMD with different THBCs and the PTC. By comparing Figs. 18–24, the 7L-THBC registers better performance compared to other THBCs (3L, 5L) and the conventional DTC drive. It may be noted that the switching power loss in the dual-inverter system is higher in the case of the 7L-THBC compared to the 3L- and 5L-THBCs and lower compared to the PTC. This fact is attributed to higher switching, which on the one hand reduces the ripple in current (and therefore torque) and on the other hand, increases the switching power loss. However, paying this price could be a justifiable proposition to improve the longevity of the bearings of the motor, and stress on the insulation. Fig. 25 shows the experimental set-up used in this paper.

VIII. CONCLUSION

This paper describes the behavior of an OEWIMD, which is controlled by both DTC technique and PTC. The shortcomings associated with the conventional DTC based on the 2L VSI are avoided by employing either multilevel THBCs or the PTC strategy.

Both simulation and experimental results suggest that the number of levels present in the THBC wield a profound influence on the performance of the DTC induction motor drives.

From the simulation and experimental results, it is evident that, though PTC results in the reduction of flux and current ripple, it also causes more power loss (i.e., the sum of switching and conduction loss) in the dual-inverter system. While the reduction of flux ripple with PTC is quite nominal, the reduction in the current ripple is quite appreciable. However, the results for the torque ripple are mixed and no definitive statement can be made in favor of any approach. The simulation and experimental results reveal that PTC for 3L OEWIMD performs much better than the conventional 2L DTC drive and even the 3L THBC DTC drive. The torque ripple with PTC is almost on par to the 7L THBC DTC drive, while it is marginally lower compared to the 5L THBC DTC drive. From these results, it is evident that neither of the approaches is all-advantaged and the multilevel THBC-DTC-based control strategy can be portrayed as a viable alternative to the PTC. Also, at low speed of operation, the 5L THBC-based DTC results in lesser fluctuations in the motor torque as well as the rotor speed.

REFERENCES

[1] S. Kouro, J. Rodriguez, B. Wu, S. Bernet, and M. Perez, "Powering the future of industry: High-power adjustable speed drive topologies," *IEEE Ind. Appl. Mag.*, vol. 18, no. 4, pp. 26–39, Jul. 2012.
[2] J. Rodríguez, J.-S. Lai, and F. Z. Peng, "Multilevel inverters: A survey of topologies, controls, and applications," *IEEE Trans. Ind. Electron.*, vol. 49, no. 4, pp. 724–738, Aug. 2002.
[3] L. G. Franquelo, J. Rodriguez, J. I. Leon, S. Kouro, R. Portillo, and M. A. M. Prats, "The age of multilevel converters arrives," *IEEE Ind. Electron. Mag.*, vol. 2, no. 2, pp. 28–39, Jun. 2008.
[4] J.-S. Lai and F. Z. Peng, "Multilevel converters—A new breed of power converters," *IEEE Trans. Ind. Appl.*, vol. 32, no. 3, pp. 509–517, May/Jun. 1996.
[5] S. Foti *et al.*, "An open-end winding motor approach to mitigate the phase voltage distortion on multilevel inverters," *IEEE Trans. Power Electron.*, vol. 33, no. 3, pp. 2404–2416, Mar. 2018.
[6] A. Edpuganti and A. K. Rathore, "Optimal pulsewidth modulation for common-mode voltage elimination scheme of medium-voltage modular multilevel converter-fed open-end stator winding induction motor drives," *IEEE Trans. Ind. Electron.*, vol. 64, no. 1, pp. 848–856, Jan. 2017.
[7] V. F. Pires, D. Foito, and J. F. Silva, "Fault-tolerant multilevel topology based on three-phase H-bridge inverters for open-end winding induction motor drives," *IEEE Trans. Energy Convers.*, vol. 32, no. 3, pp. 895–902, Sep. 2017.
[8] J. Kalaiselvi and S. Srinivas, "Bearing currents and shaft voltage reduction in dual-inverter-fed open-end winding induction motor with reduced CMV PWM methods," *IEEE Trans. Ind. Electron.*, vol. 62, no. 1, pp. 144–152, Jan. 2015.
[9] B. Mahato, R. Raushan, and K. C. Jana, "Modulation and control of multilevel inverter for an open-end winding induction motor with constant voltage levels and harmonics," *IET Power Electron.*, vol. 10, no. 1, pp. 71–79, Jan. 2017.
[10] B. P. Reddy and S. Keerthipati, "A multilevel inverter configuration for an open-end-winding pole-phase-modulated-multiphase induction motor drive using dual inverter principle," *IEEE Trans. Ind. Electron.*, vol. 65, no. 4, pp. 3035–3044, Apr. 2018.
[11] J. Kim, J. Jung, and K. Nam, "Dual-inverter control strategy for high-speed operation of EV induction motors," *IEEE Trans. Ind. Electron.*, vol. 51, no. 2, pp. 312–320, Apr. 2004.
[12] E. Levi, "Multiphase electric machines for variable-speed applications," *IEEE Trans. Ind. Electron.*, vol. 55, no. 5, pp. 1893–1909, May 2008.

[13] A. Somani, R. K. Gupta, K. K. Mohapatra, and N. Mohan, "On the causes of circulating currents in PWM drives with open-end winding AC machines," *IEEE Trans. Ind. Electron.*, vol. 60, no. 9, pp. 3670–3678, Sep. 2013.
[14] J. Hong, H. Lee, and K. Nam, "Charging method for the secondary battery in dual-inverter drive systems for electric vehicles," *IEEE Trans. Power Electron.*, vol. 30, no. 2, pp. 909–921, Feb. 2015.
[15] V. Verma and A. Kumar, "Cascaded multilevel active rectifier fed three-phase smart pump load on single-phase rural feeder," *IEEE Trans. Power Electron.*, vol. 32, no. 7, pp. 5398–5410, Jul. 2017.
[16] S. Jain, R. Karampuri, and V. T. Somasekhar, "An integrated control algorithm for a single-stage PV pumping system using an open-end winding induction motor," *IEEE Trans. Ind. Electron.*, vol. 63, no. 2, pp. 956–965, Feb. 2016.
[17] M. F. Escalante, J. C. Vannier, and A. Arzande, "Flying capacitor multilevel inverters and DTC motor drive applications," *IEEE Trans. Ind. Electron.*, vol. 49, no. 4, pp. 809–815, Aug. 2002.
[18] G. S. Buja and M. P. Kazmierkowski, "Direct torque control of PWM inverter-fed AC motors—A survey," *IEEE Trans. Ind. Electron.*, vol. 51, no. 4, pp. 744–757, Aug. 2004.
[19] S. Kouro, R. Bernal, H. Miranda, C. A. Silva, and J. Rodriguez, "High-performance torque and flux control for multilevel inverter fed induction motors," *IEEE Trans. Power Electron.*, vol. 22, no. 6, pp. 2116–2123, Nov. 2007.
[20] F. Khoucha, S. M. Lagoun, K. Marouani, A. Kheloui, and M. E. H. Benbouzid, "Hybrid cascaded H-bridge multilevel-inverter induction-motor-drive direct torque control for automotive applications," *IEEE Trans. Ind. Electron.*, vol. 57, no. 3, pp. 892–899, Mar. 2010.
[21] I. Takahashi and T. Noguchi, "A new quick-response and high-efficiency control strategy of an induction motor," *IEEE Trans. Ind. Appl.*, vol. IA-22, no. 5, pp. 820–827, Sep./Oct. 1986.
[22] M. Depenbrock, "Direct self-control (DSC) of inverter-fed induction machine," *IEEE Trans. Power Electron.*, vol. PEL-3, no. 4, pp. 420–429, Oct. 1988.
[23] T. G. Habetler, F. Profumo, M. Pastorelli, and L. M. Tolbert, "Direct torque control of induction machines using space vector modulation," *IEEE Trans. Ind. Appl.*, vol. 28, no. 5, pp. 1045–1052, Sep./Oct. 1992.
[24] J. Rodriguez and P. Cortes, *Predictive Control of Power Converters and Electrical Drives*, 1st ed. Hoboken, NJ, USA: Wiley, 2012.
[25] P. Correa, M. Pacas, and J. Rodriguez, "Predictive torque control for inverter-fed induction machines," *IEEE Trans. Ind. Electron.*, vol. 54, no. 2, pp. 1073–1079, Apr. 2007.
[26] H. Miranda, P. Cortes, J. I. Yuz, and J. Rodriguez, "Predictive torque control of induction machines based on state-space models," *IEEE Trans. Ind. Electron.*, vol. 56, no. 6, pp. 1916–1924, Jun. 2009.
[27] S. A. Davari, D. A. Khaburi, and R. Kennel, "An improved FCS–MPC algorithm for an induction motor with an imposed optimized weighting factor," *IEEE Trans. Power Electron.*, vol. 27, no. 3, pp. 1540–1551, Mar. 2012.
[28] Y. Zhang and H. Yang, "Two-vector-based model predictive torque control without weighting factors for induction motor drives," *IEEE Trans. Power Electron.*, vol. 31, no. 2, pp. 1381–1390, Feb. 2016.
[29] Y. Zhang, H. Yang, and B. Xia, "Model-predictive control of induction motor drives: Torque control versus flux control," *IEEE Trans. Ind. Appl.*, vol. 52, no. 5, pp. 4050–4060, Sep./Oct. 2016.
[30] V. P. Muddineni, A. K. Bonala, and S. R. Sandepudi, "Enhanced weighting factor selection for predictive torque control of induction motor drive based on VIKOR method," *IET Electr. Power Appl.*, vol. 10, no. 9, pp. 877–888, Nov. 2016.
[31] V. P. K. Kunisetti, R. E. K. Meesala, and V. K. Thippiripati, "Improvised predictive torque control strategy for an open end winding induction motor drive fed with four-level inversion using normalised weighted sum model," *IET Power Electron.*, vol. 11, no. 5, pp. 808–816, May 2018.
[32] K. M. R. Eswar, V. P. K. Kunisetti, and V. K. Thippiripati, "Enhanced predictive torque control for open end winding induction motor drive without weighting factor assignment," *IEEE Trans. Power Electron.*, to be published, doi: 10.1109/TPEL.2018.2812760.
[33] S. Lakhimsetty, N. Surulivel, and V. T. Somasekhar, "Improvised SVPWM strategies for an enhanced performance for a four-level open-end winding induction motor drive," *IEEE Trans. Ind. Electron.*, vol. 64, no. 4, pp. 2750–2759, Apr. 2017.
[34] P. Vas, *Sensorless Vector and Direct Torque Control* (Monographs in Electrical and Electronic Engineering). Oxford, U.K.: Oxford Univ. Press, 1998.
[35] S. Lakhimsetty and V. T. Somasekhar, "Discontinuous decoupled SVPWM schemes for a four-level open-end winding induction motor drive with waveform symmetries," *IET Power Electron.*, vol. 11, no. 2, pp. 280–292, Feb. 2018.
[36] N. Mohan, T. M. Undeland, and W. P. Robbins, *Power Electronics: Converters, Applications, and Design*, 3rd ed. Hoboken, NJ, USA: Wiley, 2003.

Suresh Lakhimsetty received the B.Tech. degree in electrical and electronics engineering from the Vignan Engineering College, Vadlamudi, India, and the M.Tech. degree from the National Institute of Technology, Calicut, India, in 2008 and 2010, respectively. He is currently pursuing the Ph.D. degree with the Department of Electrical Engineering, National Institute of Technology, Warangal, India.

His current research interests include multilevel inverters, induction motor drives, and Z-source inverters.

Venkata Siva Prasad Satelli received the M.Tech degree in power electronics and drives from the National Institute of Technology, Warangal, India, in 2017.

He is currently a Design Engineer with IE Power Technologies Private Limited, Bengaluru, India. His current research interests include electric drives, pulsewidth techniques, renewable energy sources, and active filters.

Rajendra Singh Rathore received the M.Tech. degree in power electronics and drives from the National Institute of Technology, Warangal, India, in 2017.

He is currently a RAMS Engineer with Bombardier Transportation, Hyderabad, India.

His current research interests include pulsewidth modulation techniques and induction motor drives.

V. T. Somasekhar (M'11) received the bachelor's degree from the National Institute of Technology, Warangal, India, in 1988, the master's degree from IIT Bombay, Bombay, India, in 1990, and the Ph.D. degree from (the Indian Institute of Science, Bengaluru, India, in 2003.

He was a Research and Development Engineer at M/s Perpetual Power Technologies, Bengaluru and a Senior Engineer at M/s Kirloskar Electric Co. Ltd., Mysore, India, from 1990 to 1993. He joined the Faculty of Electrical Engineering with the National Institute of Technology, in 1993, where he is currently a Professor. His current research interests include multilevel inversion with open-end winding induction motors, ac drives, and pulsewidth modulation strategies.